Vertical Velocity Structures in an Axisymmetric, Nonhydrostatic Tropical Cyclone Model

STEPHEN J. LORD AND JACQUELINE M. LORD

Hurricane Research Division/AOML/NOAA, Miami, Florida

(Manuscript received 10 June 1987, in final form 10 November 1987)

ABSTRACT

A statistical analysis of several experiments with different microphysical parameterizations in an axisymmetric, nonhydrostatic tropical cyclone model illustrates the impact of ice-phase microphysics on model vertical velocity structure. The parameterizations are designed to illustrate the effects of 1) thermodynamic input through latent heating, 2) vertical sorting of microphysical species by fallspeed, and 3) different rates of the parameterized microphysical conversion processes. The results confirm previous studies on the thermodynamic effect of melting, but they also show that the other factors, namely, fallspeed and microphysical conversion rates, are important in determining model vertical velocity structure and evolution. Statistical summaries of updrafts and downdrafts show distinct increases in the intensity and horizontal scale of downdrafts near the melting level when parameterized snow is included. Model storms without snow show a greater percentage of convective-scale updrafts and downdrafts; they intensify more slowly but ultimately become stronger than those that have larger scale vertical velocity structures.

1. Introduction

Integrations of an axisymmetric, nonhydrostatic tropical cyclone model by Willoughby et al. (1984) and Lord et al. (1984), hereafter denoted by W84 and L84 respectively, have shown that inclusion of parameterized ice-phase processes produces dramatic differences in the structure and evolution of the simulated vortex. When ice is present, the number of concentric convective rings increases and the vortex grows more slowly. Furthermore, model downdrafts are stronger, appear to be more horizontally coherent and often originate at the melting level. Low-level convergence due to horizontal spreading of downdraft air appears to be a significant forcing mechanism for the convective rings outside the eyewall. Thus the increased presence of convective rings, indirectly forced by melting of ice, has a substantial impact on the evolution of the model vortex.

Introduction of an ice-phase microphysics to the numerical model obviously involves the additional latent heat of fusion, but it also involves the addition of at least one new microphysical species with a different range of fallspeeds. Moreover, increasing the number of conversion processes among all microphysical species adds new "degrees of freedom" to the microphysical system and can modify the production rates for microphysical species (Lin et al. 1983). For example, in the ice-phase parameterization used by L84, nonprecipitating cloud ice, snow and graupel were added; the number of conversion processes increased from three in the original model without ice-phase physics to 24. These three factors, thermodynamic input through latent heating, vertical sorting of various microphysical species by different fallspeeds, and modification of microphysical conversion rates through additional processes, all contribute to the differences in model structure and evolution discussed by W84 and L84. Although W84 and L84 assessed the interaction between these factors qualitatively (e.g., the ratio of the horizontal advective speed of snow at cloud top to the mean fallspeed toward the melting level was hypothesized to determine a horizontal scale for downdrafts originating at the melting level), the emphasis was on thermodynamic effects; no attempt was made to assess the role of other factors. In this followup paper, these complicated interactions are studied further by means of several additional experiments using highly simplified ice phase parameterizations. Statistical summaries of model results over 12–24 h periods illustrate the impact of different model physics over times exceeding the lifetimes of microphysical particles and individual convective features.

In section 2, we briefly summarize the model and describe the experiments. Section 3 presents the results; section 4 gives a discussion and concluding remarks.

2. The model and experiments

a. The basic dynamical model and previous experiments

The basic dynamical model here has been described by W84. It employs the fully compressible equations

Corresponding author address: Dr. Stephen J. Lord, Environmental Research Laboratories, Hurricane Research Division/AOML, 4301 Rickenbacker Causeway, Miami, FL 33149.

of motion written in cylindrical coordinates. The prognostic variables are the radial, tangential and vertical velocities, perturbation pressure, perturbation potential temperature, various water species and the momentum diffusion coefficient. The linearized acoustic terms in the radial and vertical momentum and continuity equations are integrated with a time step of 2 s. The nonlinear (advective) forcing terms for the acoustic waves and the remaining thermodynamic, tangential wind and water species continuity equations are integrated separately with a time step of 20 s. This basic dynamical model is marched forward for 100 h over a domain of 1500 × 20 km. The model has a constant horizontal grid spacing of $\Delta r = 2$ km for $0 \leq r \leq 100$ km and a variable spacing of $2 \leq \Delta r \leq 55$ km for the remainder of the domain. The lowest model level is at $z = 100$ m; surface fluxes of sensible and latent heat are parameterized with standard bulk aerodynamic formulas (see W84). The vertical resolution is $\Delta z = 1$ km everywhere. The model begins with zero radial and vertical velocity, and a maximum tangential wind of 8 m s^{-1} at $z = 100$ m and $r = 75$ km; the mass field is in gradient and hydrostatic balance with the tangential wind field.

Previous studies described by W84 and L84 have used both a liquid water microphysics and the complete ice-phase microphysics described by L84. The most important microphysical conversion processes in these models are summarized schematically in Fig. 1. In the water model (W, Fig. 1a), cloud water and vapor interact through condensation and evaporation determined by a saturation adjustment procedure. The primary conversion of cloud water into rain is by accretion, with a rate given by (Lin et al. 1983),

$$R_{acw} = Cq_{cw}q_R^{0.95}, \quad (1)$$

where C is a constant, q_{cw} the cloud water mixing ratio and q_R the rainwater mixing ratio. Evaporation of rain gives a source for vapor to complete the water cycle. In the ice model (I, Fig. 1b), the water cycle is much more complicated, so that some less important conversion processes have been omitted for simplicity. The saturation adjustment processes of condensation, deposition, evaporation and sublimation determine the interactions among vapor, cloud ice and cloud water. The primary conversion paths are then from cloud ice and cloud water to snow by Bergeron processes and accretion, and from cloud water to snow by accretion. Snow converts to graupel by accretion. Graupel accretes rain, producing additional graupel for temperatures $T < 0$°C, and melts, forming rain for temperatures $T > 0$°C. As in W, accretion converts cloud water to rain and evaporation converts rain to water vapor.

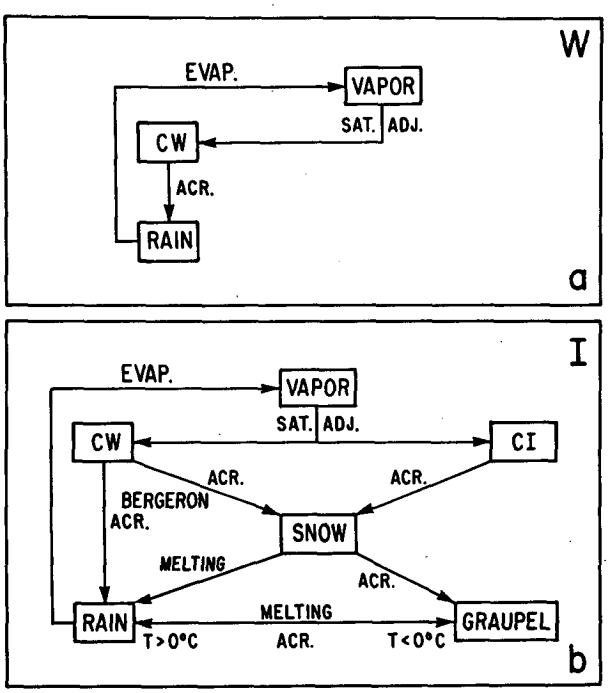

FIG. 1. Schematic diagram of parameterized microphysics for the water model [W, panel (a)] and ice model [I, panel (b)]. See text.

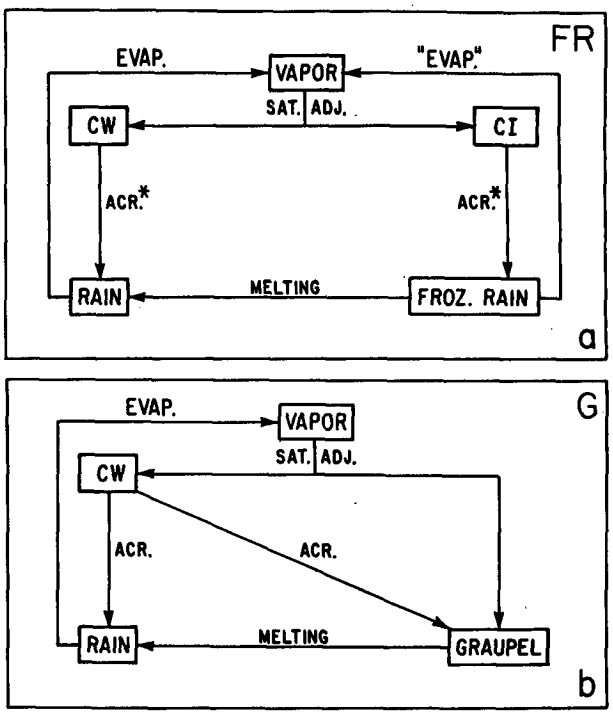

FIG. 2. As in Fig. 1, except for the "frozen rain" model [FR, panel (a)] and the "graupel" model [G, panel (b)]. Asterisk indicates the linearized form of the accretion process given by Eq. (2).

b. *Two additional experiments*

Figure 2 shows modified microphysical parameterizations for two additional experiments introduced in

this paper. The first is the "frozen rain" model (FR, Fig. 2a), in which the latent heat of fusion from freezing and melting is included, while the fallspeeds and microphysical conversion rates for the liquid water microphysics are retained as follows. There are two suspended water species, cloud water and cloud ice, and two precipitating species, rain and frozen rain, both with the same bulk formulation of fallspeed (Lin et al. 1983). Interactions between vapor, cloud water and cloud ice through saturation adjustment are identical to I, so that the latent heating by condensation and freezing is typical of I for a given vertical flux of vapor. Conversion rates of cloud water to rain and cloud ice to frozen rain are *each* determined by "linearized" forms of R_{acw} given by (1). This linearization is achieved by combining the precipitating water species into "total precipitating water" and using its concentration as the second term in (1). For accretion of cloud water and the analogous process for cloud ice, the conversion rates are

$$R^*_{acw} = Cq_{cw}q^{0.95}_{\mathrm{TPW}} \tag{2a}$$

$$F^*_{aci} = Cq_{ci}q^{0.95}_{\mathrm{TPW}}, \tag{2b}$$

where $q_{\mathrm{TPW}} = q_{\mathrm{R}} + q_{\mathrm{F}}$ is the total mixing ratio of precipitating water, q_{F} is the mixing ratio of frozen rain, the constant C is the same as in (1) and the asterisk indicates the linearization. The partition of condensate into cloud water and cloud ice, and subsequent conversion into precipitating species by (2), does not change the total conversion rate of suspended water into precipitating water. If (1) were applied separately to the two pairs q_{cw} and q_{R} and q_{ci} and q_{F}, this total conversion rate would not be maintained. Thus, model FR has been designed to incorporate the additional latent heating effect of I, while imitating the vertical sorting by fallspeed and microphysical conversion rates of W.

The second modified microphysical parameterization is for the "graupel" model (G, Fig. 2b). Albeit unrealistic, this parameterization has been designed to remove the mesoscale processes forced by the cloud ice and snow species (L84), and to enhance the cumulus scale cloud dynamical and microphysical processes such as water loading and an increased ice production rate in strong updrafts. The saturation adjustment scheme produces cloud water and, directly, a frozen, precipitating water species with the bulk fallspeed of graupel. This "graupel" grows by accreting cloud water and melts with the rates given by the full ice-phase parameterization in I. Since cloud ice and snow are not present in this model, it is anticipated that cooling due to melting should be on the cumulus scale rather than distributed horizontally over mesoscale distances of 10–30 km, as discussed in L84. Furthermore, since saturation adjustment produces a fast precipitating species, the rapid removal of water loading in updrafts and its effect on vortex evolution should be apparent.

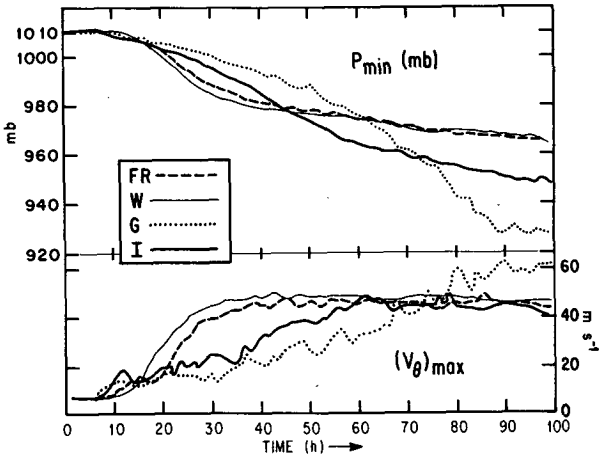

FIG. 3. Time history of minimum surface pressure (p_{min}) and maximum tangential wind [$(v_\theta)_{\mathrm{max}}$] at 3.1 km altitude for the four models, W, I, FR and G.

3. Results

a. *Time evolution and vertical structure*

The time evolutions of minimum surface pressure p_{min} and maximum tangential wind $(v_\theta)_{\mathrm{max}}$ at 3.1 km altitude for the four models W, I, FR and G are shown in Fig. 3. The results for W and I are identical to those shown in L84. The evolution of FR follows approximately midway between W and I for the first 46 h for both p_{min} and $(v_\theta)_{\mathrm{max}}$; afterward, FR closely follows W. Model G shows a completely different evolution, with a distinctly slower drop in p_{min} and lower wind speeds by approximately 10 m s^{-1} over the first 65 h. However, after that time, p_{min} decreases rapidly in comparison to the other models and $(v_\theta)_{\mathrm{max}}$ also increases rapidly. By 100 h, p_{min} = 926 mb, compared to 947 mb for I, 964 for FR and 965 mb for W. Models FR and W behave somewhat similarly, whereas I and G show much slower drops in p_{min} and growth of $(v_\theta)_{\mathrm{max}}$.

Typical, instantaneous radius-height distributions of vertical velocity are shown in Fig. 4. At the times shown, the models are all at approximately the same intensities as measured by p_{min} and $(v_\theta)_{\mathrm{max}}$. In W (Fig. 4a) a single, outward-sloping eyewall with an area of mesoscale ascent extending 20–30 km outward from the eyewall is the dominant feature in the vertical velocity field. In I, an outward-sloping eyewall in the lower troposphere becomes more vertical above 6 km. An outer convective ring is present at 50–55 km radius and an area of mesoscale ascent at 60–70 km is located radially outward from the convective ring. Downdrafts in I tend to originate at the melting level and are stronger and more horizontally coherent than in W. More detailed description of models W and I are found in L84.

The vertical velocity distribution of model FR exhibits an interesting double eyewall structure. The inner

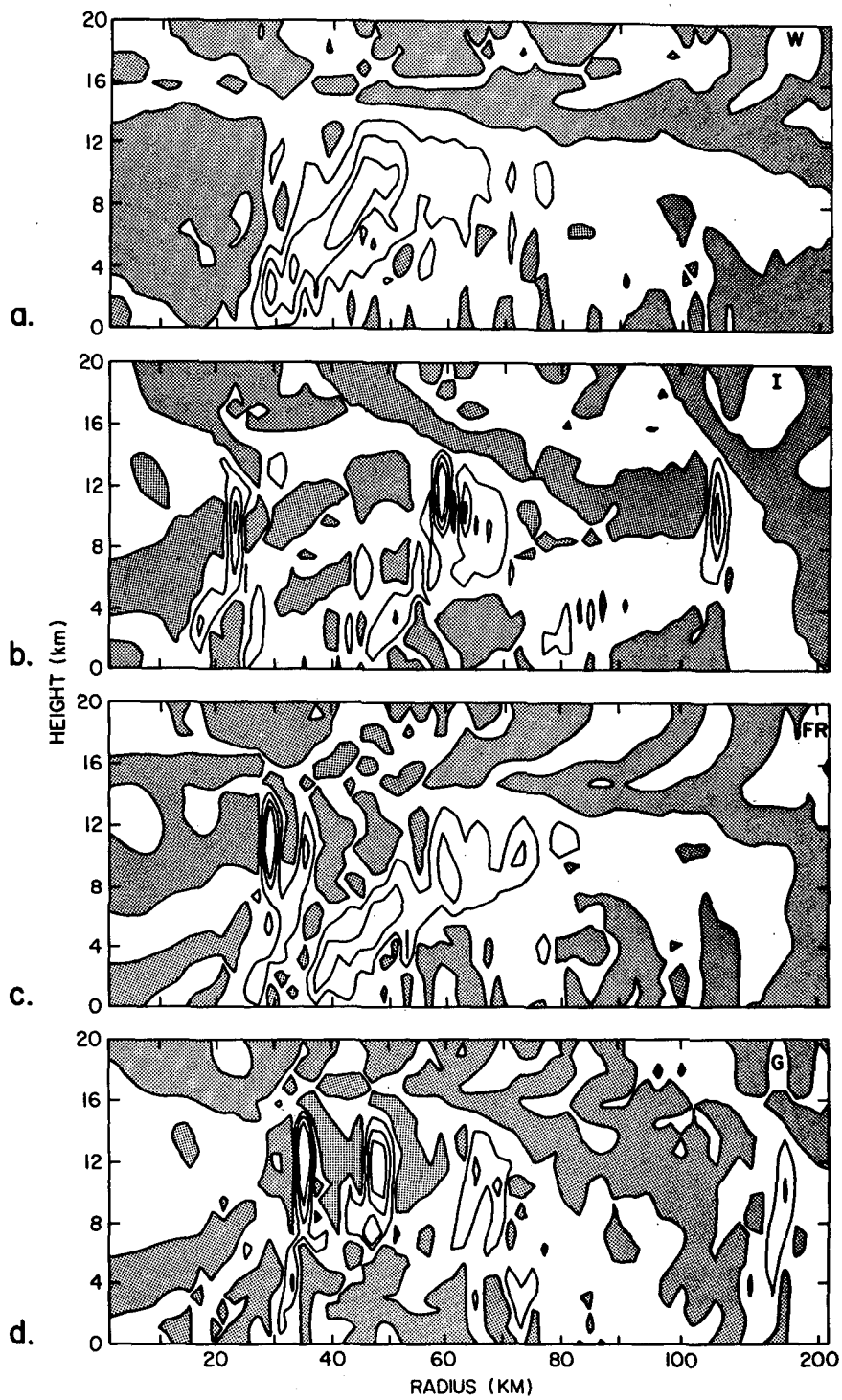

FIG. 4. Typical instantaneous radius–height distributions of vertical velocity over the inner 200 km for models W (22:00), I (36:00), FR (23:00), and G (43:00). Times (hh:mm) for each model are in parentheses. Note that the region $100 \leq r \leq 200$ km is compressed due to the expanding grid size. Isolines are 0, 1, 2.5 and 4 m s^{-1} and negative values are stippled.

eyewall, at radius r = 25–33 km, is narrow and slopes outward below 5–6 km, but is vertically oriented above. This eyewall closely resembles the one in I in magnitude and orientation, except that the downdraft just outside the eyewall is not as well developed. The outer eyewall, from 37–55 km, closely resembles the eyewall in W in

width and outward slope with height, and also in the area of mesoscale updraft outside the eyewall in the upper troposphere. There is some tendency for downdrafts to initiate near the melting level (e.g., at r = 55–67 km), but this tendency is not as strong as in I. In model G, updrafts are very narrow with noticeably less outward slope in the lower troposphere than in any of the other models. Downdrafts are also more frequent. They appear most often directly beneath the strongest middle and upper tropospheric updrafts. They are narrow, vertically oriented, and do not often originate near the melting level as in I. When significant updrafts occur over mesoscale regions in the upper troposphere (at r = 60–70 km), they originate from the merging of narrow convective updrafts instead of from horizontal spreading of a single updraft as in I (see L84 for a more complete discussion).

The radius–height distributions of rainwater are shown in Fig. 5. Both models W and FR exhibit 20–30 km wide regions of $q_R > 2$ g kg^{-1}, whereas models I and G show much narrower rainshafts with lower q_R. The wider rainshafts in W and FR derive from outward advection of cloud water from the major updrafts at high levels. Since the cloud water is suspended, it can be carried horizontally for relatively large distances before being converted to rain and precipitating. In this case, where suspended water species comprise a large part of the condensate and the conversion to precipitating species is relatively slow, the horizontal extent of the rainshafts is determined by the outflow speed in the upper troposphere and the rate of conversion from cloud water to rain. The rapid decrease in q_R above ~5 km in I shows that above the freezing level ice processes are very efficient at removing liquid water (see L84). However, where updrafts are more vigorous (as in G at $r \sim 35$ km), rain may be carried considerably higher. The very narrow, vertically oriented, rainshafts in G are a direct consequence of eliminating the cloud ice and snow species from this model. Conversion of all frozen water to fast-falling graupel unloads the updrafts, making them more vigorous and more vertical; rapid conversion of cloud water to graupel removes cloud water before it can be advected radially outward, so that little horizontal spreading of rain occurs. In I, horizontal spreading can occur due to the presence of cloud ice and snow, but since snow also precipitates, the rainshafts are not as narrow as those in G, but narrower than those in both W and FR.

b. Updraft and downdraft statistics

Statistical summaries of model updrafts and downdrafts from the four model runs, W, I, FR and G were obtained from model output sampled over the convectively active region $20 \leq r \leq 100$ km in each model for various time periods (Table 1). These periods contain the typical model structures shown in Figs. 4–5. At 20 min intervals (three per hour of model time) a 5 min average of vertical velocity was calculated at each grid point within the sampling domain. These average vertical velocities were then sorted by intensity and horizontal scale as described below. Tests with higher density sampling did not change the results significantly.

1) INTENSITY

Figure 6 shows the frequency distribution of updraft and downdraft intensity with height for each model. Each vertical velocity sample was sorted according to intensity from $-5 \leq w \leq 15$ m s^{-1}. Separate categories were created for downdrafts with $w < -5$ m s^{-1} and updrafts with $w > 15$ m s^{-1}. The numbers of drafts in each category were then expressed as a percentage of all sampled drafts. For W (Fig. 6a), the percentage of updrafts in the range $0.5 \leq w \leq 5$ m s^{-1} increases with height from 1–5 km, thereby indicating an increasing updraft intensity with height *on the average.* Intensities of the strongest updrafts do not exceed 10 m s^{-1}. Furthermore, they show a relatively uniform distribution with height compared with weak updrafts. Downdraft intensities are quite uniform with height and do not exceed -5 m s^{-1}. The frequency distribution for I (Fig. 6b) is quite different from that of W. For I, the strongest updrafts increase with height above about 6 km, whereas in W the distribution is uniform with height. The most striking feature for I is that the stronger downdrafts with $w < -0.3$ m s^{-1} are considerably more frequent below the melting level (~5 km) than above. There is also a minimum in the frequency of 1 m s^{-1} updrafts near the melting level.

The statistics for FR generally have the same characteristics as those of I, but with some significant differences. Although stronger downdrafts are more frequent in both I and FR, they are not as frequent in FR. The strongest updrafts in I are at higher levels than in FR. In G, both updrafts and downdrafts tend to be stronger than in any of the other models. Some updrafts exceed 15 m s^{-1} and downdrafts exceed -5 m s^{-1} above 10 km. Frequencies of moderate downdrafts (approximately -2 m s^{-1}) are also increased relative to the other models. There is only a slight increase in downdraft intensity near the freezing level, but the decreased intensity of weak updrafts is similar to I and FR.

2) HORIZONTAL EXTENT

Frequency distributions of the horizontal extent of downdrafts and updrafts are shown in Figs. 7–8. Here, horizontal extent E is defined as the horizontally contiguous domain over which the 5 min averaged vertical velocity maintains the same sign and exceeds a given threshold. The purpose of the threshold is to filter out small amplitude motions that are always present in the model; the thresholds are $w = -0.1$ m s^{-1} for downdrafts and $w = 0.5$ m s^{-1} for updrafts. The results shown

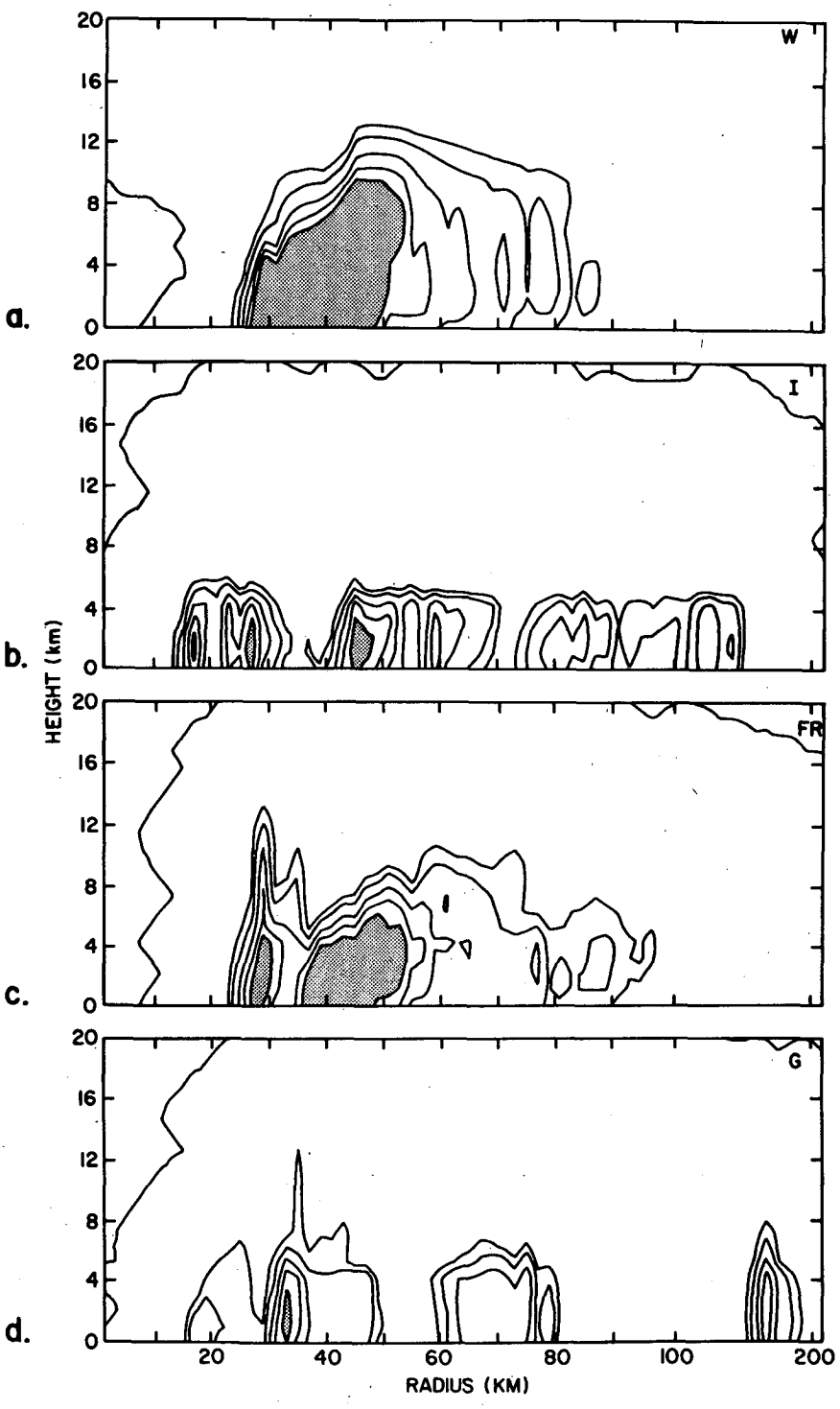

FIG. 5. As in Fig. 4, except for rainwater mixing ratio. Isolines are 0.0, 0.25, 0.5, 1.0, 1.5 and 2.0 g kg^{-1}. Values greater than 2 g kg^{-1} are stippled.

in Figs. 7–8 are not sensitive to the exact choice of threshold. Downdrafts of larger horizontal extent in I (Fig. 7b) are more frequent at and below the melting level; this effect is not so apparent in FR and G and, of course, not present at all in W. At convective scales ($E < 5$ km), the distribution of updraft horizontal extent (Fig. 8) shows very few differences among the models, but some differences occur on the mesoscale

TABLE 1. Sampling period (hh:mm) used to derive updraft and downdraft statistics for each model.

Model	Sampling period
W	12:00–29:40
I	27:00–46:00
FR	16:00–40:40
G	35:00–60:00

($E > 30$ km). Both W and FR have a higher frequency of mesoscale updrafts in the upper troposphere ($\sim$12 km) that does not occur in I and G, although there is a slight tendency in I for an increase of E = 10–15 km updrafts in this region. Examples of these mesoscale updrafts are shown in Fig. 4a and 4c. The larger frequency of mesoscale updrafts occurs in the models with microphysical conversion rates typical of W. These updrafts are absent in G, where rapid accretion by graupel and rain reduces the cloud water concentrations and rainshafts are comparatively narrow (Fig. 5d). The differences in vertical structure shown statistically in Figs. 6–8 will be interpreted further in the next section.

4. Discussion and concluding remarks

In this section we discuss the foregoing results in light of the three factors introduced by the addition of ice-phase microphysics to the tropical cyclone model: thermodynamic input through latent heating, vertical sorting by different fallspeed, and microphysical conversion rates. Since these factors are manifested in complicated nonlinear interactions between the model's dynamic and thermodynamic processes, these discussions are necessarily qualitative.

a. Thermodynamic input

Comparison of models W and FR, in which microphysical fallspeeds and conversion rates are the same but with latent heating from freezing and melting added in FR, shows that the thermodynamic input *by itself* is a noticeable, but secondary effect. It does not result in a significant change in the eventual intensity of the modeled storm, nor does it modify the evolution significantly (Fig. 3). While there is some enhancement of downdrafts in FR by cooling due to melting (Fig. 6), this effect does not force long-term changes in the convective structure; outer convective rings resemble those of W rather than those of I (Fig. 4). Indeed, models W and FR demonstrate that other dynamical and microphysical factors besides thermodynamic input must be operating in order to produce the large differences in model structure and evolution between W and I discussed by W84 and L84.

b. Vertical sorting of microphysical species by fallspeed

The influence of vertical sorting can most easily be seen by comparing the results of FR and G. These models differ primarily in that G has no cloud ice species. Therefore, condensate falls more rapidly from updrafts in G than in FR. As a result, stronger updrafts are statistically more frequent in G than in any other model (Fig. 6). Furthermore, strong middle and upper-

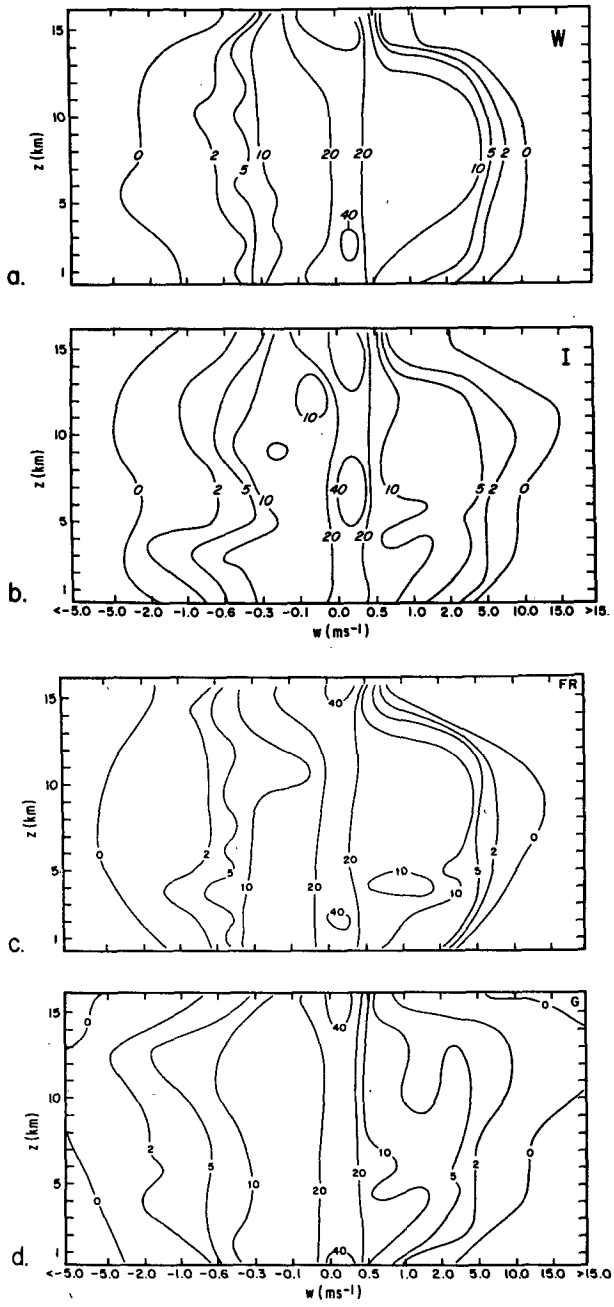

FIG. 6. Frequency distribution (%) of updraft ($w > 0$) and downdraft ($w < 0$) intensity vs. height Z (km) for models W, I, FR and G (panels a–d, respectively).

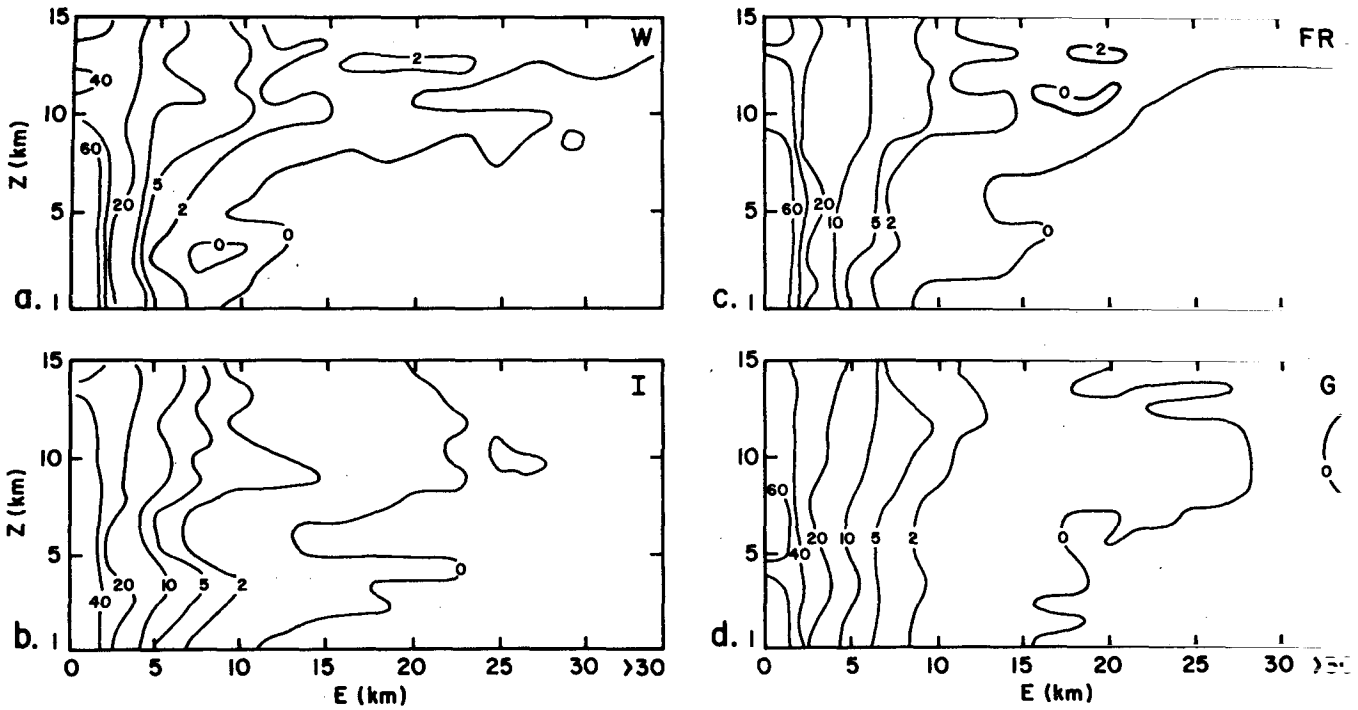

FIG. 7. Frequency distribution (%) of downdraft horizontal extent E (km) vs. height Z (km) for models W, I, FR and G (panels a–d, respectively). See text for definition of E.

tropospheric downdrafts are more frequent, partly because they are forced by precipitation drag and partly because strong upper-level updrafts and inertial stability of the simulated vortex together force local descent. It is interesting that there is very little evidence of enhanced downdrafts at the melting level in G. Therefore,

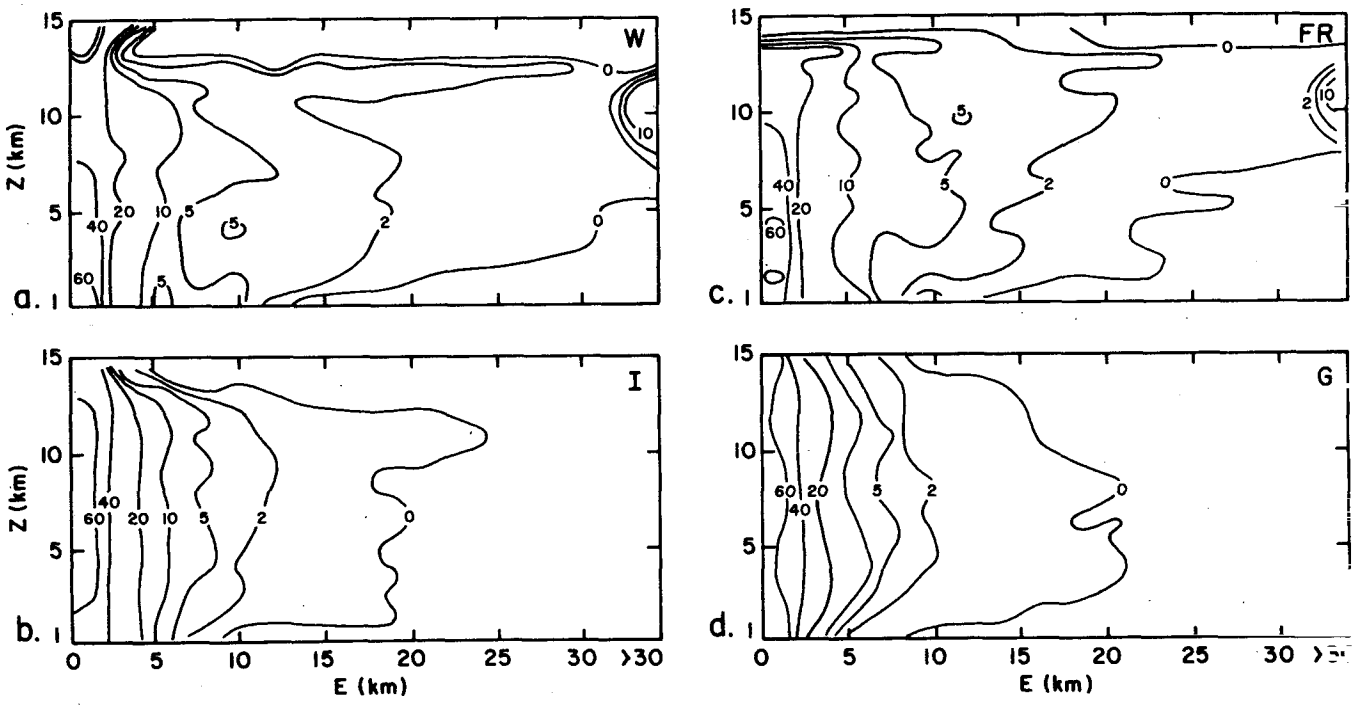

FIG. 8. As in Fig. 7 except for updraft horizontal extent.

convective-scale downdrafts in the lower troposphere are driven primarily by precipitation drag and melting is a secondary process in G.

The presence of the parameterized snow phase, which has fallspeeds of 1–2 m s^{-1}, plays a significant role in the structure and evolution of the simulated vortex as shown by W84 and L84. Although melting is included in both FR and G, these models exhibit less evidence of this process [for example, the enhancement of downdraft intensity (Fig. 6)] than in I. In FR, absence of the snow phase means that the suspended cloud ice remains in the upper troposphere for comparatively long periods of time until it is finally converted to frozen rain by the relatively slow parameterized accretion process. During this time, the cloud ice advects radially outward from the storm center over correspondingly longer distances. Precipitating ice is, therefore, spread over a larger horizontal area than it would be if cloud ice were converted to precipitating snow as in I. Thus, conversion of nonprecipitating cloud ice to precipitating snow is undoubtedly one factor that enhances the role of melting by increasing the supply of ice at the melting level. In G, cloud ice is absent; condensate converts to fast-falling graupel in close proximity to the cloud updrafts. Large fallspeeds preclude horizontal spreading of frozen condensate and, therefore, the melting effect is also not very apparent.

c. *Microphysical conversion processes*

The rapid conversion of cloud ice and cloud water to graupel in G prevents horizontal spreading of the melting process by increasing the percentage of rapidly precipitating condensate. Updrafts and downdrafts in G are not only the strongest but also the most narrow and vertically oriented of all the models discussed here. Almost all drafts are convective-scale; the possibility of mesoscale structures has been reduced by elimination of a slowly falling ice species and the extreme rapidity of frozen precipitation production in G. Formation of outer convective rings (not shown) by strong convective downdrafts is more prevalent than in I. These rings block the inward penetration of high angular momentum air and result in slower initial growth of the vortex (Fig. 3). The rings are also responsible for enhanced upward vertical transport of boundary layer air with higher angular momentum in the outer regions of the vortex. As the model integration proceeds, this model produces the strongest storm, perhaps as a result of midlevel inflow of this high angular momentum air. While the specific dynamical events that lead to the stronger model storm are difficult to analyze, our results show that, in two dimensions, different representation of microphysical processes can influence model evolution.

In conclusion, by drastic modification of parameterized microphysics, the complicated interplay of latent heating, precipitation loading of downdrafts and updrafts, and conversion of suspended condensate to precipitation has been demonstrated. These factors conspire to modify the structure and evolution of simulated tropical cyclone vortices over times that are much longer than the lifetimes of the microphysical particles themselves. Marks and Houze (1987) have demonstrated that in nature, particles of different fallspeeds can have quite different trajectories through a hurricane. The results presented here indicate the variety of dynamical and thermodynamical factors that may influence storm intensity and evolution in very subtle ways.

Acknowledgments. We thank Drs. F. D. Marks, L. J. Shapiro, H. E. Willoughby and E. Zipser for comments on this manuscript and Dr. S. L. Rosenthal for both his comments and administrative support of this research. Comments from an anonymous reviewer are appreciated. D. A. Senn and A. J. Ramsay provided graphics support.

REFERENCES

Lin, Y.-L., R. D. Farley and H. D. Orville, 1983: Bulk parameterization of the snow field in a cloud model. *J. Climate Appl. Meteor.*, **22**, 1065–1092.

Lord, S. J., H. E. Willoughby and J. M. Piotrowicz, 1984: Role of a parameterized ice-phase microphysics in an axisymmetric, nonhydrostatic tropical cyclone model. *J. Atmos. Sci.*, **41**, 2836–2848.

Marks, F. D., Jr., and R. A. Houze, Jr., 1987: Inner core structure of Hurricane Alicia from airborne Doppler radar observations. *J. Atmos. Sci.*, **44**, 1296–1317.

Willoughby, H. E., H.-L. Jin, S. J. Lord and J. M. Piotrowicz, 1984: Hurricane structure and evolution as simulated by an axisymmetric, nonhydrostatic numerical model. *J. Atmos. Sci.*, **41**, 1169–1186.